Mechanism of NAIP–NLRC4 inflammasome activation revealed by cryo-EM structure of unliganded NAIP5

Bhaskar Paidimuddala [1,4], Jianhao Cao [1,4], Grady Nash[1], Qing Xie[1], Hao Wu [2,3] & Liman Zhang [1] ✉

The nucleotide-binding domain (NBD), leucine rich repeat (LRR) domain containing protein family (NLR family) apoptosis inhibitory proteins (NAIPs) are cytosolic receptors that play critical roles in the host defense against bacterial infection. NAIPs interact with conserved bacterial ligands and activate the NLR family caspase recruitment domain containing protein 4 (NLRC4) to initiate the NAIP–NLRC4 inflammasome pathway. Here we found the process of NAIP activation is completely different from NLRC4. Our cryo-EM structure of unliganded mouse NAIP5 adopts an unprecedented wide-open conformation, with the nucleating surface fully exposed and accessible to recruit inactive NLRC4. Upon ligand binding, the winged helix domain (WHD) of NAIP5 undergoes roughly 20° rotation to form a steric clash with the inactive NLRC4, which triggers the conformational change of NLRC4 from inactive to active state. We also show the rotation of WHD places the 17–18 loop at a position that directly bind the active NLRC4 and stabilize the NAIP5–NLRC4 complex. Overall, these data provide structural mechanisms of inactive NAIP5, the process of NAIP5 activation and NAIP-dependent NLRC4 activation.

The nucleotide-binding domain (NBD), leucine rich repeat (LRR) domain containing protein family (NLR family) comprises a group of fascinating proteins that play multiple roles in the immune system[1,2]. The NLR apoptosis inhibitory proteins (NAIPs) and NLR family caspase recruitment domain containing protein 4 (NLRC4) initiate inflammation through the NAIP-NLRC4 inflammasome pathway. In this pathway, NAIP is the receptor of a bacterial ligand to mount inflammation against pathogenic Gram-negative bacteria, such as *Legionella pneumophila* and *Salmonella typhimurium*[3]. There are multiple NAIP proteins in mice. Among them, NAIP2 recognizes the Rod proteins such as *Salmonella* PrgJ, NAIP5 and NAIP6 recognize Flagellin proteins such as *Salmonella* FliC or *Legionella* FlaA, and NAIP1 recognizes Needle proteins such as *Salmonella* PrgI[4–6]. Unlike in mice, there is only one NAIP protein present in humans (hNAIP). It has the same domain organization as mNAIPs, but

may respond to all three bacterial ligands[7]. After activation, NAIPs can activate NLRC4 and form the wheel-like NAIP–NLRC4 inflammasome complex, which further recruits and activates the effector protein pro-caspase-1 (refs. [8–12]).

Structurally, the NBD, together with helical domain 1 (HD1), winged helix domain (WHD) and helical domain 2 (HD2), forms the ATPase domain in both NAIP and NLRC4. At the N-terminal end, NAIPs have three baculovirus inhibitor of apoptosis protein repeat (BIR) domains, whereas NLRC4 contains a caspase recruitment domain (CARD), which binds pro-caspase-1 CARD through the CARD-CARD interaction[13–17]. NAIP5 binds flagellin through extensive interactions with the N-terminal helix (NTD), BIR1, HD1, HD2 and LRR domains, and adopts an open conformation similar to that of NLRC4 in the inflammasome complex[18–20]. One single copy of ligand-bound NAIP initiates

[1]Department of Chemical Physiology and Biochemistry, Oregon Health and Science University (OHSU), Portland, OR, USA. [2]Department of Biological Chemistry and Molecular Pharmacology, Harvard Medical School, Boston, MA, USA. [3]Program in Cellular and Molecular Medicine, Boston Children's Hospital, Boston, MA, USA. [4]These authors contributed equally: Bhaskar Paidimuddala, Jianhao Cao. ✉e-mail: zhanglim@ohsu.edu

NAIP−NLRC4 assembly by inducing in NLRC4 a roughly 90° rotation of the WHD−HD2−LRR domains to expose the nucleating surface in the NBD, which further converts more NLRC4 molecules from their closed auto-inhibited state to an open, activated, oligomeric state[14,15].

Previous studies have greatly enhanced our knowledge of the NAIP−NLRC4 inflammasome in bacterial defense. However, our understanding of NAIP regulation remains limited, mostly due to a lack of structural information on inactive NAIP. NAIPs share the domain organization of NLRC4, except for the N-terminal part. Therefore, inactive NAIPs were proposed to adopt an auto-inhibited conformation similar to the inactive NLRC4 (refs. [14,15,18,19]). However, mutations that break the auto-inhibition of NLRC4 are related to auto-inflammatory diseases[8,21], while no mutations on NAIPs have been identified to cause auto-inflammatory diseases, to our best knowledge. This may be either because auto-activation of NAIP is lethal, or inactive NAIPs might have unique features that prevent them from auto-activation. Here we report the cryo-EM structure of unliganded NAIP5, and the conformational change during NAIP5 activation, which provide multiple insights into the structural basis of NAIP−NLRC4 inflammasome activation.

Results

Cryo-EM structure determination of unliganded NAIP5

We expressed recombinant full-length NAIP5 with an N-terminal Flag tag from Expi293F cells, and purified it with anti-Flag affinity purification followed by size-exclusion chromatography (SEC). The protein elutes as two peaks from Superdex 200, including a void peak showing irregular aggregation under negative staining EM, and an 11.5 ml peak that contains well dispersed particles (Extended Data Fig. 1). The fractions from the 11.5 ml peak were then combined, concentrated and loaded back to SEC followed by multi-angle light scattering (MALS). The elution volume of the concentrated protein remained unchanged from SEC−MALS, with a detected molecular weight corresponding to monomeric NAIP5, indicating the 11.5 ml fraction is the NAIP5 monomer (Fig. 1a and Extended Data Fig. 1). We then performed structural analysis with the 11.5 ml peak fractions. Cryo-EM data were collected using a Titan Krios microscope equipped with a K3 direct detector, obtaining 3,682 micrographs at 0° tilt and 1,597 micrographs at 30° tilt. After multiple rounds of two-dimensional (2D) classification, ab initio reconstruction and heterogeneous refinement with cryoSPARC and Relion[22,23], a final particle set containing 122,990 at 0° tilt and 36,523 at 30° tilt was obtained for nonuniform refinement, resulted a 3.3 Å density map (Fig. 1b,c, Extended Data Fig. 2 and Table 1).

For model building, we first attempted to fit the AlphaFold predicted model of mouse NAIP5 into the cryo-EM map[24]. Even though the N-terminal domains of the AlphaFold model fit in well, a mismatch starting from the WHD domain occurred, indicating conformational difference. The AlphaFold model was then split into individual domains and fitted separately into the density map. The domains are then connected and refined by multiple rounds of real space refinement in Coot and Phenix[18,19,25,26].

Overall, our map has well resolved density in the BIR1, BIR2, BIR3, NBD, HD1, WHD and a main part of the HD2 regions, but the N-terminal helix (residues 1–46), a loop of BIR3 (287–294), the linker between BIR3 and NBD (residues 351–399), the inserted helix in HD2 (residues 818–856) and the C-terminal part of the LRR domain (residues 916–980, 1,076–1,403) are missing (Fig. 1c and Extended Data Fig. 3). Plotting the missing regions of the NAIP5[unliganded] model onto the two published NAIP5[liganded] structures showed that they are mostly involved in NAIP5-flagellin interactions, indicating the dynamic nature of these regions may be functionally important for ligand recognition (Fig. 1e).

During cryo-EM data processing, we found homogeneous refinement in cryoSPARC produced a lower resolution map but maintained longer LRR density (Fig. 1d and Extended Data Fig. 2a,c), so we attempted to fit the LRR fragment (1,076–1,403) from the AlphaFold model into the

cryo-EM map of homogeneous refinement, and found only one potential direction that the LRR segment could fit (Fig. 1d). For the convenience of discussion, we rigidly placed the LRR fragment into the homogeneous refinement map, generating the model of NAIP5[unliganded (LRR+)] (Fig. 1d). The unliganded NAIP5 does not form the closed, auto-inhibited structure as observed in inactive NLRC4 (Fig. 1f)[13]. Rather, it adopts a wide-open conformation that is further extended from the active conformation of NAIP5 in the NAIP−NLRC4 inflammasome complex[14,15,18,19], hereinafter called the wide-open conformation (Fig. 1g). The different inactive conformations of NAIP5 and NLRC4 indicate the molecular mechanism underlying their activation may also be different, despite their shared conserved domain organization.

BIR domains and the nucleotide-binding pocket

The two published NAIP5[liganded] structures (hereafter cited with their Protein Data Bank (PDB) IDs 5YUD and 6B5B, respectively) traced the BIR2 and BIR3 domains differently. When BIR1 is aligned, BIR3 in 6B5B is located at the tip of the molecule, while BIR2 was not observed. In 5YUD, BIR2 is at the tip of the molecule and BIR3 is located in the back. Our NAIP5[unliganded] map has reliable density in the linkers connecting BIR1−BIR2−BIR3, which supports BIR2 residing at the tip and BIR3 in the back (Fig. 1c and Extended Data Fig. 3).

Our cryo-EM map also shows clear density corresponding to ATP in the nucleotide-binding pocket, coordinated by NBD, HD1 and WHD, despite the absence of exogenous nucleotides added during purification (Fig. 2a,b). This indicates that ATP, rather than ADP, binds strongly to unliganded NAIP5. ATP density was also observed in active NAIP5 in 5YUD (ref. [19]). Superimposition of the ATP binding pocket of NAIP5[unliganded] and 5YUD showed most residues in ATP binding remain in the same place, except K678 and Y679, which moved away from the ATP molecule on NAIP5 activation (Fig. 2b). To test whether this movement has functional consequences, we mutated K678 and Y679 to L (KY2L). The protein was neither auto-activated in the absence of ligand, nor deficient in IL-1β processing when ligand was added, indicating the interactions of these two residues with ATP is neither required for maintaining NAIP5 inactive conformation, nor for inflammasome activation (Fig. 2c). Moreover, NAIP5 only showed slow ATPase activity (ATP was hydrolyzed at a rate of 2.2 ± 0.2 molecules per molecule of NAIP5 per hour at 25 °C) (Fig. 2d), which was not enhanced by *Salmonella* FliC (Fig. 2e and Extended Data Fig. 1f). Together, these data agree with the structure, and indicate that the ligand-dependent activation of NAIP5 may not be accompanied by ATP hydrolysis, or ATP/ADP exchange, hence differing from other AAA+ ATPases[2,27−31].

Conformational change in the WHD−HD2−LRR domains

We analyzed the conformational change of NAIP5 on flagellin binding by superimposing the structures of NAIP5[unliganded] and NAIP5[liganded] (PDB 6B5B and 5YUD). When the NBDs of the three structures are aligned, both BIR1 and HD1 are aligned well, indicating that there is little conformational change in these domains (BIR2 and BIR3 domains are skipped as they were not well resolved in PDB 5YUD and 6B5B) (Fig. 2f). However, starting from the very beginning of WHD, the liganded conformation in both 6B5B and 5YUD rotates roughly 20° from the unliganded conformation, resulting in movement in the α14 helix, a turn in the middle of the α15 helix and movement in α16−α18 helixes in the WHD domain (Fig. 2g). Compatible with the WHD movement, the HD2 and LRR domains also rotate from the unliganded to the liganded conformation, making NAIP5[liganded] less extended than NAIP5[unliganded] (Figs. 1g and 2h). Since both HD2 and LRR have extensive interactions with flagellin in the ligand-bound NAIP5 (Figs. 1e and 2h), we propose that flagellin binding may directly drive the HD2−LRR movement, which then induces the conformational change of WHD.

The nucleating surface is exposed in the unliganded NAIP5

Structural alignment of NAIP5[unliganded] and NAIP5[liganded] provided multiple insights into the process of NAIP5 activation and NAIP5-dependent
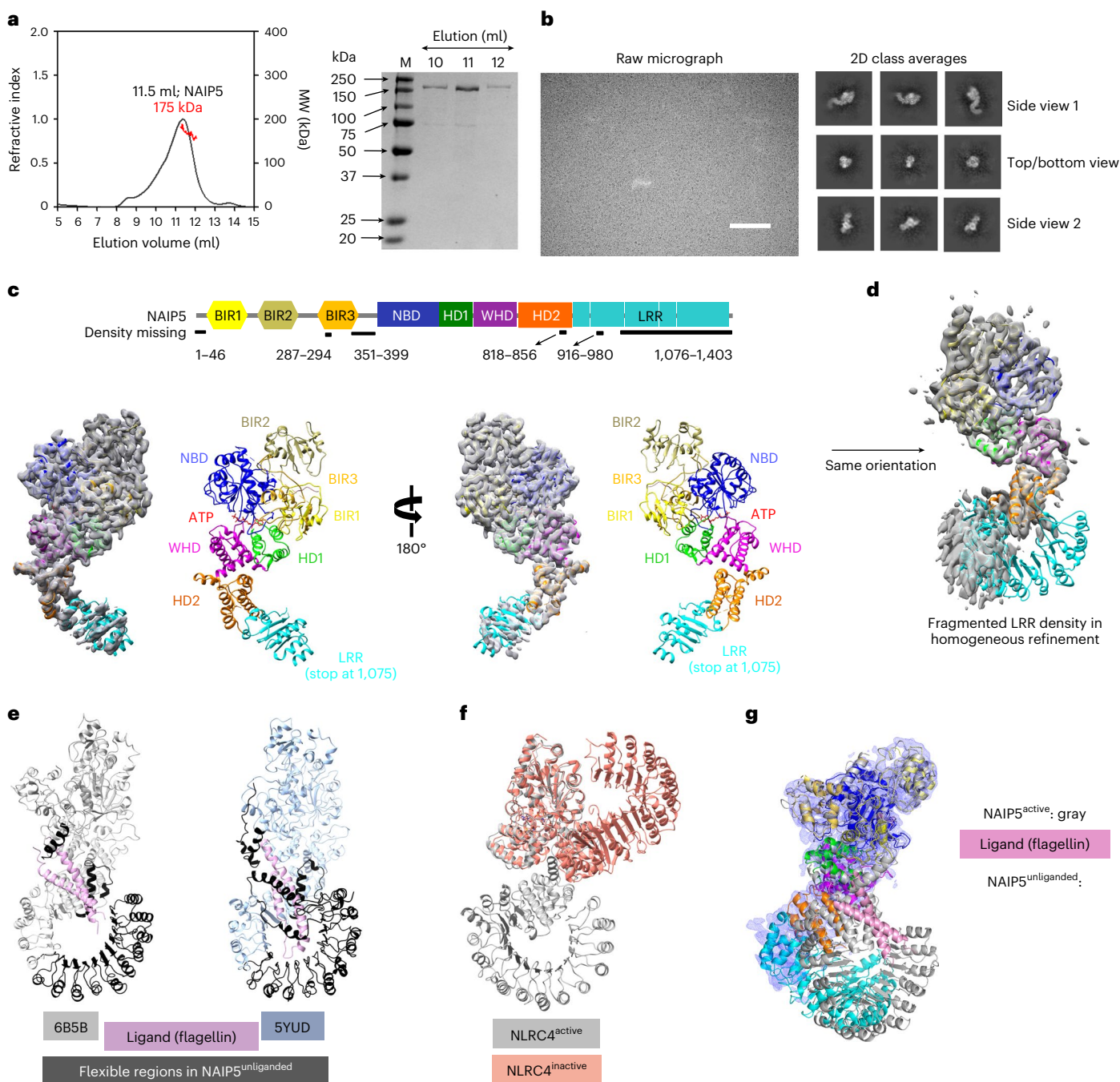
Fig. 1 | Biochemical purification and cryo-EM structure of NAIP5. a, MALS measurement of the NAIP5-11.5 ml peak fractions from SEC and SDS–PAGE of these fractions. This experiment was repeated three independent times. MW, molecular weight. **b**, A representative cryo-EM micrograph and 2D class averages showing the side view and top/bottom views. Scale bar, 100 nm. **c**, Domain organization, cryo-EM map and ribbon diagram of unliganded NAIP5, individual domains are color coded and missing densities are labeled. **d**, Homogeneous refinement map with improved LRR density. **e**, Missing densities (black) are plotted in the two published active NAIP5 structures (PDB 6B5B and 5YUD). **f**, Overlay of NLRC4inactive and NLRC4active structure. **g**, Overlay of NAIP5unliganded and NAIP5active structure. As the overall structure of active NAIP5 revealed by 5YUD and 6B5B is similar, only 6B5B is shown in this figure. Flagellin that binds with NAIP5active is in pink, and cryo-EM density of NAIP5unliganded is in blue mesh. Color coding as in **c**.

NLRC4 activation. Here we start our discussion from the NBD domain. Previous cryo-EM studies showed that the NBD of NAIP5liganded and NLRC4active bear a conserved positively charged nucleating surface, which is critical for both NAIP-dependent and NLRC4-dependent NLRC4 activation (Extended Data Fig. 4a,c)[14,15]. In comparison, the nucleating surface of NLRC4inactive is embedded by the intramolecular interactions between NBD–LRR domains, which prevents auto-activation of NLRC4 (Extended Data Fig. 4b). It was proposed that in the process of NAIP-dependent NLRC4 activation, the nucleating surface of NAIP5liganded binds to the receptor surface of NLRC4inactive and triggers the NLRC4 conformational change, this can expose the nucleating surface of NLRC4 to recruit the next inactive NLRC4, eventually forming NLRC4 oligomers (Extended Data Fig. 4e)[14,15,18,19].

The nucleating surface is completely exposed in our structure of NAIP5unliganded and resembles the NAIP5liganded structures in this region (Fig. 2f and Extended Data Fig. 4c,d). As unliganded NAIP5 cannot form a detectable complex with the nucleating surface mutated NLRC4 (NSM), or induce wild-type (WT) NLRC4 oligomerization (Extended Data

Table 1 | Cryo-EM data collection, refinement and validation statistics

	Unliganded NAIP5
	(EMDB-24387, EMDB-24389), (PDB 7RAV)
Data collection and processing	
Magnification	81,000
Voltage (kV)	300
Electron exposure (e⁻/Å²)	52
Defocus range (μm)	1.0 to 2.5
Pixel size (Å)	0.5347
Symmetry imposed	C1
Initial particle images (no.)	8,044,442
Final particle images (no.)	159,513
Map resolution (Å)	3.3 (EMDB-24387)
	3.6 (EMDB-24389)
FSC threshold	0.143
Refinement	
Initial model used (PDB code)	PDB 6B5B, 5YUD, AlphaFold (AF-Q9R016-F1-model_v1)
Model resolution (Å)	3.8
FSC threshold	0.5
Map sharpening B factor (Å²)	171.9
Model composition	
Nonhydrogen atoms	6,215
Protein residues	773
Ligands	ATP: 1
B factors (Å²)	
Protein	93.79
Ligand	76.02
R.m.s. deviations	
Bond lengths (Å)	0.005
Bond angles (°)	1.157
Validation	
MolProbity score	2.46
Clashscore	16.0
Poor rotamers (%)	1.80
Ramachandran plot	
Favored (%)	82.88
Allowed (%)	16.73
Disallowed (%)	0.39

Fig. 4f)[4,28], this observation indicates the exposed nucleating surface per se is not sufficient for NAIP5 to activate NLRC4. This suggests the molecular mechanism of ligand-driven NAIP5 activation is not to break a presumably auto-inhibited conformation to expose its nucleating surface, as in NLRC4 activation. How, then, is NAIP5 activated on ligand binding?

Conformational changes in NAIP5^WHD activate NLRC4

To understand how the exposed nucleating surface of NAIP5^unliganded is prevented from activating NLRC4, we built models of the hypothetical encounter complexes formed by either pre- or postliganded NAIP5 with inactive NLRC4 by aligning the nucleating surface of these structures to their corresponding subunits in the active inflammasome complex

(PDB 6B5B) (Extended Data Fig. 4e)[14,18]. We then superimposed models of the NAIP5^unliganded–NLRC4^inactive and NAIP5^liganded–NLRC4^inactive by aligning the NBDs of NAIP5 subunits (Fig. 3). In the NAIP5^liganded–NLRC4^inactive complex, the 16–17 loop and 17–18 loop in the WHD domain of NAIP5^liganded exert steric clash with NLRC4^inactive, which may push the WHD of NLRC4 to initiate NLRC4 conformational change. However, the 16–17 loop in the WHD domain of NAIP5^unliganded is further back relative to the position of NLRC4^inactive (Fig. 3a), while 17–18 loop is further down (Fig. 3b), and neither of these loops form a steric clash with NLRC4^inactive. This explains that while NAIP5^unliganded may transiently recruit inactive NLRC4, it cannot activate it, suggesting the occurrence of steric clash between the WHD domains of active NAIP5 and inactive NLRC4 is essential for inflammasome activation. Superimposition of complexes formed by active NLRC4 with pre- or postliganded NAIP5 showed that the activated NLRC4 can establish new interactions with the 15–16 and 17–18 loops of liganded NAIP5, whereas it clashes with the same loops in the unliganded form (Fig. 3c).

The 17–18 loop is essential for NAIP−NLRC4 activation

As discussed, the 17–18 loop in active NAIP5 not only forms a steric clash with inactive NLRC4 to drive its conformational change (Fig. 3b), but also interacts with NLRC4^active (Fig. 3c). While single-site mutations on the 15–16 loop (E707R) and the 17–18 loop (Q735A) mediated IL-1β processing similar to WT NAIP5, the level of IL-1β processing was greatly reduced by the 17–18 loop deletion (Dloop, deletion of Q735, R736, L737, R738 in the 17–18 loop) (Fig. 3d). The 17–18 loop deletion also abolished NLRC4 oligomerization on blue native–PAGE (Fig. 3e). Pulldown experiments showed the Dloop mutation eliminated the interaction between NAIP5 and NLRC4 in the presence of FliC (Fig. 3f). Altogether, these data showed the 17–18 loop is essential for NAIP−NLRC4 complex formation and inflammasome activation. Because the 17–18 loop is involved in several steps of inflammasome activation, the defective IL-1β processing from the Dloop mutation may be a result of both reduced steric clash with inactive NLRC4 (Fig. 3b) and reduced interaction with active NLRC4 (Fig. 3c).

Mutations in NAIP5-LRR do not impair inflammasome activation

Active NAIP5 also interacts with active NLRC4 in the LRR regions (Fig. 3g), but the functional importance of this interaction has not been extensively investigated. Previous study showed deletion of the NLRC4-LRR auto-activates the inflammasome[13], indicating its interaction with NAIP5 in the inflammasome complex may not be essential. Even though the LRR region in our NAIP5^unliganded structure is poorly resolved, it is clear that it is neither in the orientation that masks NBD (as in the NLRC4 auto-inhibited conformation), nor in the orientation that can interact with active NLRC4 (as in the inflammasome disk) (Figs. 2h and 3g). To further understand the function of LRR interactions in NAIP−NLRC4 activation, we tested the effect of NAIP5^LRR mutations on IL-1β processing. Inflammasome assays showed none of the tested LRR mutations (Q1348A, DM (double mutant, Q1339A, T1342A) and QTT3A (a combination of Q1339A, T1341A and T1342A)) had a notable effect on IL-1β processing, suggesting the LRR interaction between NAIP5^liganded and NLRC4^active is not critical for inflammasome assembly in the over-expression system (Fig. 3g,h).

Altogether, even though the nucleating surface, 15–16 loop, 17–18 loop and LRR of NAIP5 are all involved in NAIP5-NLRC4 interaction in the active state, only the nucleating surface and 17–18 loop are important in the formation of the functional inflammasome complex (Extended Data Fig. 5).

Revised model of NAIP5 and NAIP5-dependent NLRC4 activation

With these observations, we propose a new model for NAIP5 activation and NAIP5-dependent NLRC4 activation. Before ligand stimulation, NAIP5^unliganded and NLRC4^inactive may exist as either individual proteins, or a transient complex through the exposed NAIP5-nucleating surface. Flagellin binding induces the HD2 and LRR regions of NAIP5 to move
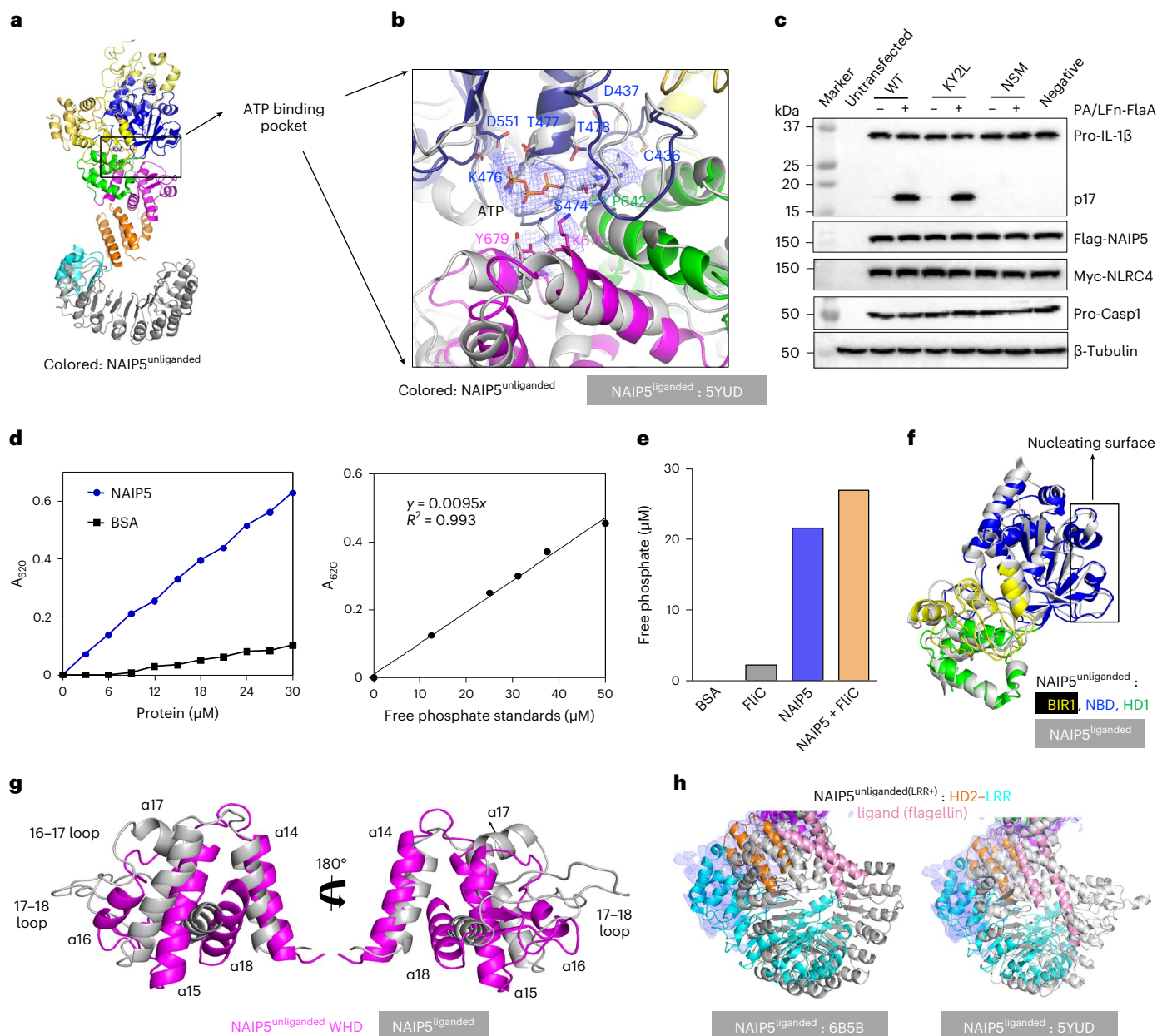
Fig. 2 | ATP binding and the conformational change on NAIP5 activation. **a**, The ATP binding pocket in NAIP5^{unliganded}, colored as in Fig. 1c. The missing fragment in LRR is colored in gray. **b**, Superimposition of ATP binding pocked of the unliganded (colored) and postliganded (gray) conformation. **c**, KY2L does not affect the IL-1β processing in the presence and absence of flagellin; NAIP5–NSM and PA/LFn-FlaA-AAA (negative) that are defective in activating inflammasome were used as negative controls. This experiment was repeated three independent times. **d**, NAIP5 shows weak ATPase activity. This experiment was repeated three independent times. **e**, The ATPase activity of NAIP5 is not enhanced by flagellin (FliC). This experiment was repeated three independent

times, and one repetition of this experiment with separately purified batches of protein is shown in Extended Data Fig. 1f. **f**, Superimposition of NAIP5–BIR1–NBD–HD1 in the unliganded (colored) and postliganded (gray) conformation. As PDB 5YUD and 6B5B are similar in these regions, only 6B5B is shown in this figure. **g**, Superimposition of NAIP5–WHD in the unliganded (magenta) and postliganded (gray) conformation. As 5YUD and 6B5B are similar in WHD, only 6B5B is shown in this figure. **h**, Superimposition of NAIP5–HD2, LRR in the unliganded (colored) and postliganded (gray) conformation; both published NAIP5^{liganded} structures are shown as the LRR domains are traced differently in these two models.

from the inactive position to the active position, which results in the conformational change in the WHD. After activation, the 16–17 loop and 17–18 loop in the NAIP5–WHD domain form steric clash with NLRC4^{inactive} to promote it to open up, and the 17–18 loop of NAIP5 then binds to activated NLRC4 to stabilize the NAIP5^{liganded}–NLRC4^{active} complex (Fig. 4a, and Supplementary Video 1).

In our model, NAIP activation does not take place by breaking the auto-inhibition to expose the nucleating surface as in what happens in NLRC4 (Fig. 4b). Instead, it may occur on building a conformation that both allows the WHD domain to form steric clash with the unbound

inactive NLRC4, and places the WHD 17–18 loop in the right position to bind to the activated NLRC4 and stabilize the NAIP5^{liganded}–NLRC4^{active} complex (Fig. 4c). Therefore, we name our NAIP activation model the 'build to activate' model, and the previously proposed model the 'break to activate' model.

Discussion
Our model points to the importance of the NAIP5–WHD domain in successful inflammasome activation due to its roles in driving NLRC4 conformational change and stabilizing the inflammasome complex.
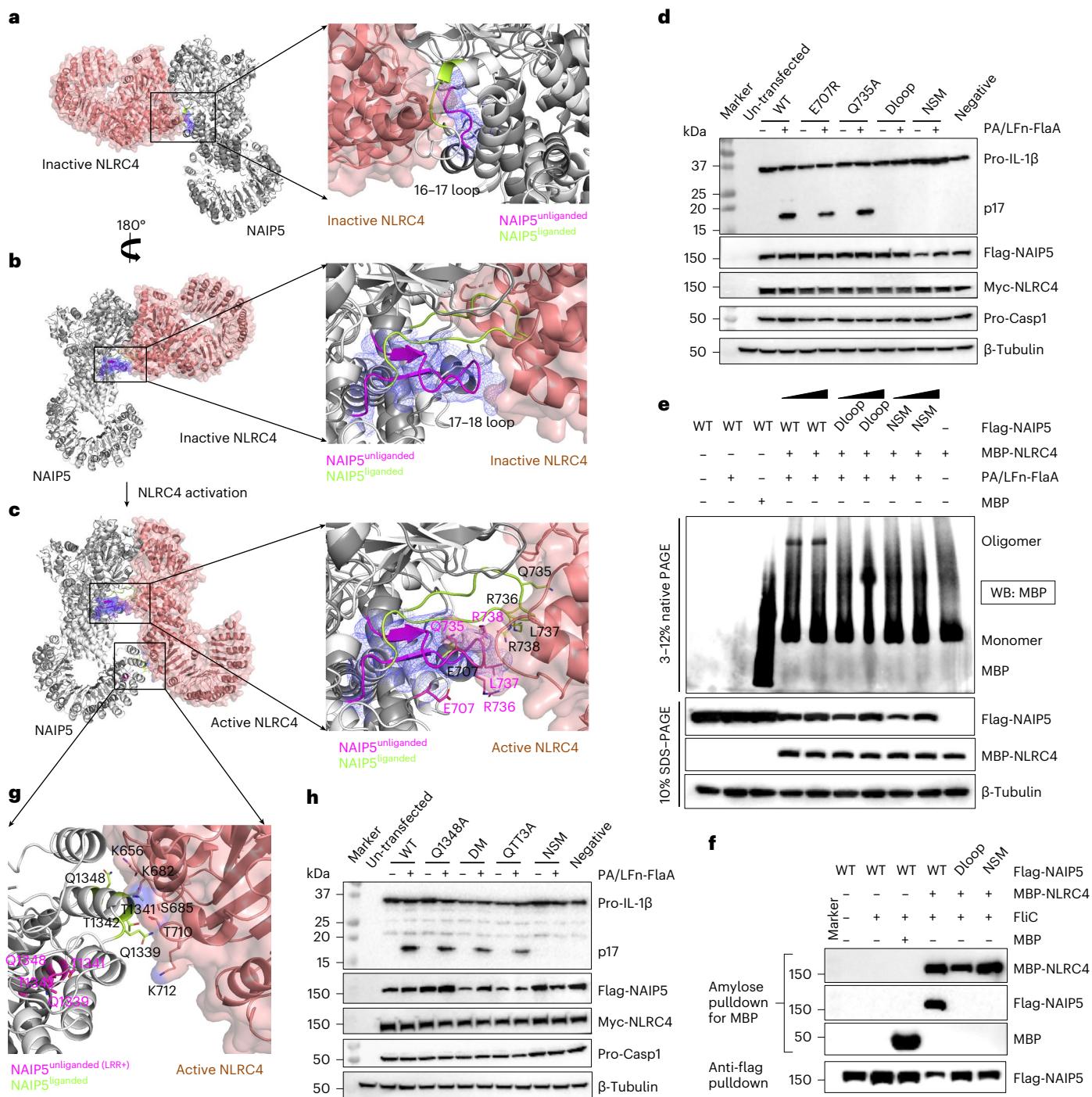
Fig. 3 | Structural basis of ligand-induced NAIP5 activation. a, The encounter complex formed by NAIP5^{unliganded}–NLRC4^{inactive} and NAIP5^{liganded}–NLRC4^{inactive}. NLRC4 is shown in salmon, NAIP5^{unliganded} in dark gray and NAIP5^{liganded} in light gray. The 16–17 loop is enlarged and highlighted. Magenta shows NAIP5^{unliganded}, lime shows NAIP5^{liganded}. **b**, 180° rotation of **a**, the 17–18 loop is enlarged and highlighted. **c**, The NAIP5–NLRC4 complex after NLRC4 is activated. the 15–16 loop and 17–18 loop is enlarged and highlighted. **d**, IL-1β processing is abolished by 17–18 loop deletion (Dloop, deletion of Q735, R736, L737, R738 in 17–18 loop). NAIP5–NSM and PA/LFn-FlaA-AAA (negative) that are defective in activating inflammasome were used as negative controls. This experiment was repeated three independent times. **e**, The 17–18 loop deletion abolished the ability of

NAIP5 to nucleate NLRC4 oligomerization; NAIP5–NSM that is defective in activating inflammasome was used as negative control. This experiment was repeated three independent times. **f**, 17–18 loop deletion reduced the NAIP5-NLRC4 interaction. This experiment was repeated three independent times. **g**, Interactions between NAIP5^{liganded} and NLRC4^{active} in the LRR domain. As PDB 5YUD and 6B5B are similar in relevant regions, only 6B5B is used to make this figure. **h**, LRR mutations have negligible effect on inflammasome activation. DM, Q1339A and T1342A double mutant; QTT3A, Q1339A, T1341A and T1342A. NAIP5–NSM and PA/LFn-FlaA-AAA (negative) that are defective in activating inflammasome were used as negative controls. This experiment was repeated three independent times.

Compared with the auto-inhibited conformation, the wide-open conformation of inactive NAIP5 provides a large open space around the HD2–LRR region to allow ligand binding. This is appealing because it affords a mechanism for the immune system to balance between stability and sensitivity. During formation of the inflammasome, a single activated NAIP protein initiates NLRC4 polymerization in a domino-like
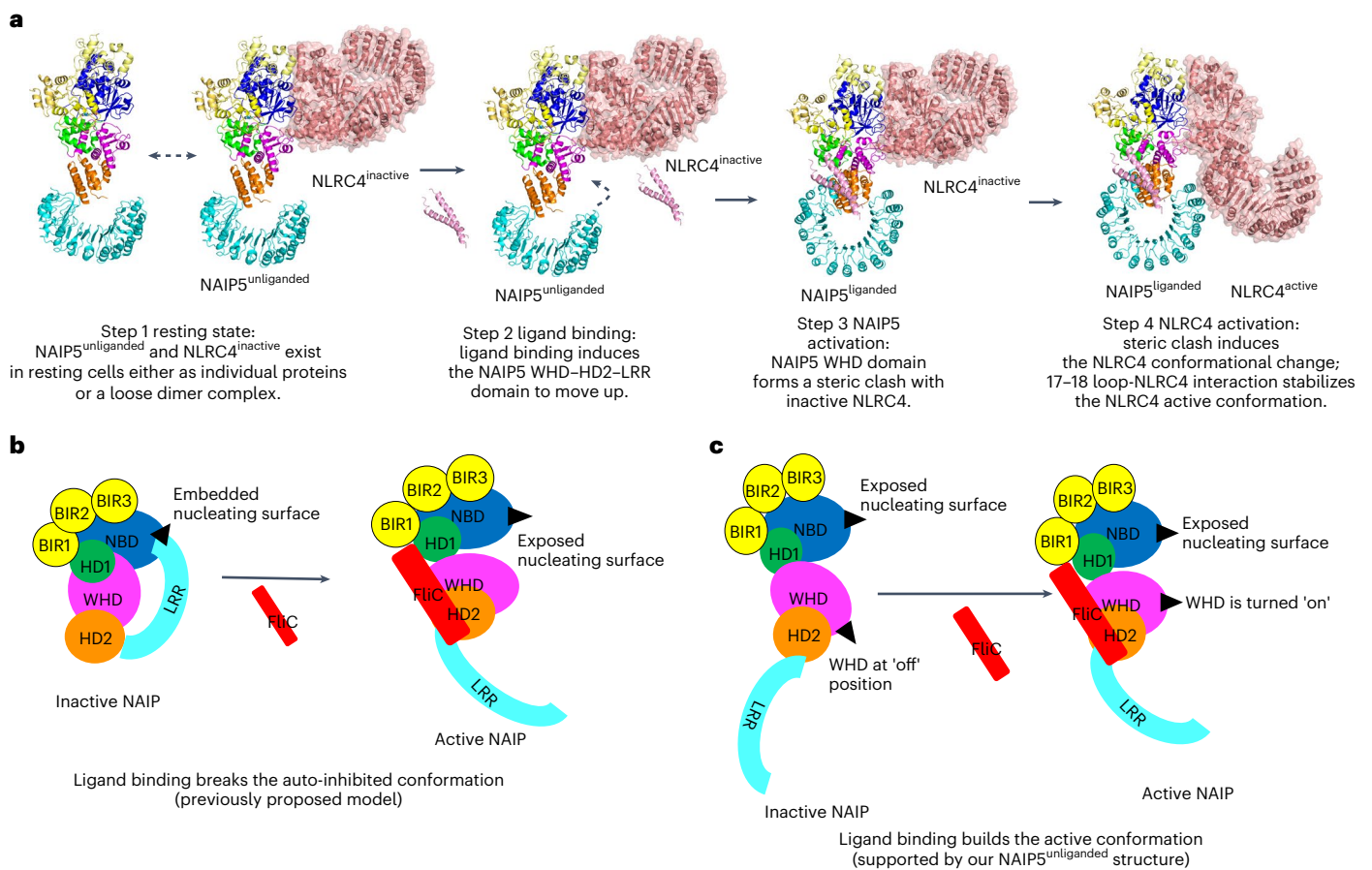
Fig. 4 | NAIP5 activation and NAIP5-triggered NLRC4 activation. a, The molecular events in NAIP5 activation and NLRC4 activation. **b**, Previously proposed auto-inhibition model in NAIP5 activation (the 'break to activate' model). In this model, ligand binding breaks the interaction between NBD and LRR region and exposes the nucleating surface. **c**, The 'build to activate' model in NAIP5 activation. In this model, ligand binding induces the movement of WHD–HD2–LRR regions to build the active NAIP5 conformation.

reaction to promote the disk assembly. As the first responder in the inflammasome pathway, the inactive conformation of the NAIP protein must be well maintained to prevent auto-activation. In the 'build to activate' model, NAIP activation is mediated by extensive interactions between inactive NAIP and its specific ligand, and it is less likely that a point mutation can cause NAIP auto-activation. This mechanism may provide a safeguard system against accidental activation of NAIP, and an explanation for why genetic studies only identified mutations on NLRC4, but not on NAIP, in human auto-inflammatory diseases[9].

It is also surprising to see that NAIP5 binds with ATP before ligand binding, as the reported auto-inhibited NLR structures of NLRC4, Apaf1, NOD2, ZAR and NLRP3 all have ADP bound to maintain the inactive form[13,32–37]. However, our structure of NAIP5 is not in an auto-inhibited conformation, and ATP binding does not trigger NAIP5 oligomerization, which is distinct from other NLRs. Although we have checked all of our fractions from SEC and did not find any 2D classes that represent a fully auto-inhibited state, we cannot exclude the possibility that an auto-inhibited state may exist. Overall, our unliganded structure strongly suggests NAIP adopts a stable wide-open conformation that has not been observed in other NLRs.

Online content

Any methods, additional references, Nature Portfolio reporting summaries, source data, extended data, supplementary information, acknowledgements, peer review information; details of author contributions and competing interests; and statements of data and code availability are available at https://doi.org/10.1038/s41594-022-00889-2.

References

1. Harton, J. A., Linhoff, M. W., Zhang, J. & Ting, J. P. Cutting edge: CATERPILLER: a large family of mammalian genes containing CARD, pyrin, nucleotide-binding, and leucine-rich repeat domains. *J. Immunol.* **169**, 4088–4093 (2002).
2. Proell, M., Riedl, S. J., Fritz, J. H., Rojas, A. M. & Schwarzenbacher, R. The Nod-like receptor (NLR) family: a tale of similarities and differences. *PLoS ONE* **3**, e2119 (2008).
3. Rauch, I. et al. NAIP proteins are required for cytosolic detection of specific bacterial ligands in vivo. *J. Exp. Med.* **213**, 657–665 (2016).
4. Kofoed, E. M. & Vance, R. E. Innate immune recognition of bacterial ligands by NAIPs determines inflammasome specificity. *Nature* **477**, 592–595 (2011).
5. Zhao, Y. et al. The NLRC4 inflammasome receptors for bacterial flagellin and type III secretion apparatus. *Nature* **477**, 596–600 (2011).
6. Yang, J., Zhao, Y., Shi, J. & Shao, F. Human NAIP and mouse NAIP1 recognize bacterial type III secretion needle protein for inflammasome activation. *Proc. Natl Acad. Sci. USA* **110**, 14408–14413 (2013).
7. Reyes Ruiz, V. M. et al. Broad detection of bacterial type III secretion system and flagellin proteins by the human NAIP/NLRC4 inflammasome. *Proc. Natl Acad. Sci. USA* **114**, 13242–13247 (2017).
8. Duncan, J. A. & Canna, S. W. The NLRC4 inflammasome. *Immunological Rev.* **281**, 115–123 (2018).

9.   Bauer, R. & Rauch, I. The NAIP/NLRC4 inflammasome in infection and pathology. *Mol. Asp. Med.* **76**, 100863 (2020).

10. Miao, E. A. et al. Innate immune detection of the type III secretion apparatus through the NLRC4 inflammasome. *Proc. Natl Acad. Sci. USA* **107**, 3076–3080 (2010).

11. Broz, P. & Dixit, V. M. Inflammasomes: mechanism of assembly, regulation and signalling. *Nat. Rev. Immunol.* **16**, 407–420 (2016).

12. Miao, E. A. et al. Cytoplasmic flagellin activates caspase-1 and secretion of interleukin 1beta via Ipaf. *Nat. Immunol.* **7**, 569–575 (2006).

13. Hu, Z. et al. Crystal structure of NLRC4 reveals its autoinhibition mechanism. *Science* **341**, 172–175 (2013).

14. Hu, Z. et al. Structural and biochemical basis for induced self-propagation of NLRC4. *Science* **350**, 399–404 (2015).

15. Zhang, L. et al. Cryo-EM structure of the activated NAIP2-NLRC4 inflammasome reveals nucleated polymerization. *Science* https://doi.org/10.1126/science.aac5789 (2015).

16. Wu, H. Higher-order assemblies in a new paradigm of signal transduction. *Cell* **153**, 287–292 (2013).

17. Li, Y. et al. Cryo-EM structures of ASC and NLRC4 CARD filaments reveal a unified mechanism of nucleation and activation of caspase-1. *Proc. Natl Acad. Sci. USA* **115**, 10845–10852 (2018).

18. Tenthorey, J. L. et al. The structural basis of flagellin detection by NAIP5: a strategy to limit pathogen immune evasion. *Science* **358**, 888–893 (2017).

19. Yang, X. et al. Structural basis for specific flagellin recognition by the NLR protein NAIP5. *Cell Res.* **28**, 35–47 (2018).

20. Zhang, L. & Wu, H. Bad germs are trapped. *Cell Res.* **28**, 141–142 (2018).

21. Canna, S. et al. A157: macrophage activation syndrome-like illness due to an activating mutation in NLRC4. *Arthritis Rheumatol.* **66**, S203 (2014).

22. Scheres, S. H. RELION: implementation of a Bayesian approach to cryo-EM structure determination. *J. Struct. Biol.* **180**, 519–530 (2012).

23. Punjani, A., Rubinstein, J. L., Fleet, D. J. & Brubaker, M. A. cryoSPARC: algorithms for rapid unsupervised cryo-EM structure determination. *Nat. Methods* **14**, 290–296 (2017).

24. Jumper, J. et al. Highly accurate protein structure prediction with AlphaFold. *Nature* **596**, 583–589 (2021).

25. Emsley, P., Lohkamp, B., Scott, W. G. & Cowtan, K. Features and development of Coot. *Acta Crystallogr. Sect. D., Biol. Crystallogr.* **66**, 486–501 (2010).

26. Afonine, P. V. et al. Real-space refinement in PHENIX for cryo-EM and crystallography. *Acta Crystallogr. D. Struct. Biol.* **74**, 531–544 (2018).

27. Halff, E. F. et al. Formation and structure of a NAIP5-NLRC4 inflammasome induced by direct interactions with conserved N- and C-terminal regions of flagellin. *J. Biol. Chem.* **287**, 38460–38472 (2012).

28. Tenthorey, J. L., Kofoed, E. M., Daugherty, M. D., Malik, H. S. & Vance, R. E. Molecular basis for specific recognition of bacterial ligands by NAIP/NLRC4 inflammasomes. *Mol. Cell.* https://doi.org/10.1016/j.molcel.2014.02.018 (2014).

29. Poyet, J. L. et al. Identification of Ipaf, a human caspase-1-activating protein related to Apaf-1. *J. Biol. Chem.* **276**, 28309–28313 (2001).

30. White, S. R. & Lauring, B. AAA+ ATPases: achieving diversity of function with conserved machinery. *Traffic* **8**, 1657–1667 (2007).

31. Maharana, J., Panda, D. & De, S. Deciphering the ATP-binding mechanism(s) in NLRP-NACHT 3D models using structural bioinformatics approaches. *PLoS ONE* **13**, e0209420 (2018).

32. Maekawa, S., Ohto, U., Shibata, T., Miyake, K. & Shimizu, T. Crystal structure of NOD2 and its implications in human disease. *Nat. Commun.* **7**, 11813 (2016).

33. Yuan, S. & Akey, C. W. Apoptosome structure, assembly, and procaspase activation. *Structure* **21**, 501–515 (2013).

34. Pang, Y. et al. Structure of the apoptosome: mechanistic insights into activation of an initiator caspase from *Drosophila*. *Genes Dev.* **29**, 277–287 (2015).

35. Sharif, H. et al. Structural mechanism for NEK7-licensed activation of NLRP3 inflammasome. *Nature* https://doi.org/10.1038/s41586-019-1295-z (2019).

36. Wang, J. et al. Reconstitution and structure of a plant NLR resistosome conferring immunity. *Science* https://doi.org/10.1126/science.aav5870 (2019).

37. Wang, J. et al. Ligand-triggered allosteric ADP release primes a plant NLR complex. *Science* **364**, eaav5868 (2019).

Methods

Plasmid construction and stable cell line generation

The pCMV-Flag-NAIP5, pBackman-MBP-NLRC4 (delta CARD) and pCMV-His-FliC plasmids were generated in our previous study[15]. Site directed mutagenesis were performed with Q5 DNA polymerase (NEB no. M0491) using the QuikChange method. To develop the stable human embryonic kidney 293F (HEK293F)-NAIP5 cell line, the sequence encoding Flag-NAIP5 from pCMV-Flag-NAIP5 was subcloned into pcDNA3.4 (Invitrogen) using the transfer PCR method[38], generating the pcDNA3.4-Flag-NAIP5 plasmid. Stable cell lines were generated following the manufacturer's instructions.

Plasmids pET15b-LFn-Fla (Addgene no. 84871), pET15-LFn-FlaAAA (Addgene no. 84872) and pET22b-PA-His (modified from Addgene no. 84863) were gifted by R. Vance[3].

Recombinant protein expression and purification

Recombinant expression of NAIP5 was carried out by either transiently transfecting Expi293F cells (Thermo Fisher no. A14635) grown in suspension culture using polyethylenimine (PEI) (Polysciences no. 23966) reagent, or directly purified from a homemade HEK293F cell line stably expressing NAIP5 protein.

For transient transfection, plasmid DNA (pCMV-Flag-NAIP5) solution was prepared by addition of 500 µg DNA to 10 ml of Opti-MEM, and PEI solution was prepared by addition of 1.5 ml of PEI (1 mg ml^{-1}) to 10 ml of Opti-MEM, and then both solutions were mixed thoroughly (DNA:PEI ratio, 1:3) and incubated for 30 min at room temperature before slowly pouring into a culture flask (0.5 l of Expi293F at 3 million cells per ml), while gently swirling. Cells were then cultivated at 125 rpm, 37 °C, 5% CO$_2$, 90% humidity for 3 days and gathered by centrifugation (JLA-8.1 fixed-angle rotor, Beckman) at 4,000g for 30 min at 4 °C. The resulting cell pellet was washed once with ice-cold PBS, flash frozen in liquid nitrogen and stored at −80 °C until use.

All purification steps were performed at 4 °C. On the day of purification, the cell pellet was thawed, resuspended in TBS buffer (50 mM Tris-HCl pH 8.0, 200 mM NaCl) with freshly added 1% Triton-X-100, 10 µg µl^{-1} DNase I (ThermoScientific no. 90083) and protease inhibitor cocktail (Sigma no. S8830), sonicated (2 s on, 6 s off, 3 min total on, 50% amplitude, Branson) and then ultra-centrifuged (200,000g, 1 h, Type 45 Ti fixed-angle rotor, Beckman). After centrifugation, the collected supernatant was incubated with anti-flag M2 affinity resin (Millipore-Sigma no. A2220, 0.5 ml, preequilibrated in TBS) for 2 h at constant rotational shaking. The mixture was then subjected to gravity flow and washed with 100 column volumes (CV) of TBS. The bound Flag-NAIP5 was eluted with TBS containing 100 µg ml^{-1} 3× Flag peptide (Sigma no. F4799) in 0.5 ml fractions. Eluted fractions containing Flag-NAIP5 were pooled, concentrated with an Amicon Ultra Centrifugal filter unit (4 ml, molecular weight cutoff 30 kDa, MilliporeSigma) to 1 ml and applied to Superdex 200 Increase 10/300 GL SEC column (Cytiva) equilibrated in TBS, eluates were collected in 0.2 ml fractions. The fractions corresponding to monomeric Flag-NAIP5 were collected and subjected to a second round of gel filtration that was connected to a MALS detector. The final purified flag-NAIP5 concentration was calculated using its predicted molar extinction coefficient and absorbance was measured at 280 nm using NanoDrop One (ThermoScientific).

LFn-FlaA, LFn-FlaAAA and protective antigen were expressed and purified as previously described with some modifications[3,5]. Briefly, the transformed *Escherichia coli* LOBSTR BL21 cells (Kerafast no. EC1002) were grown in Luria-Bertani medium containing ampicillin (100 µg ml^{-1}) until OD$_{600}$ reached to 0.8, induced with 0.5 mM IPTG and incubated at 18 °C, 200 rpm for 18 h. All purification steps were carried out at 4 °C. The collected bacterial cell pellet was resuspended in TBS buffer containing 5% glycerol, 1 mM PMSF, sonicated (2 s on, 6 s off, 5 min total on, 50% amplitude, Branson) and centrifuged (40,000g, 1 h, JA-20 fixed-angle rotor, Beckman). The collected supernatant was incubated with Ni-NTA resin (preequilibrated in TBS; Qiagen no.

30230) for 1 h at constant rotational shaking. The supernatant was removed and beads were subjected to three washes (25 CV each): TBS, TBS + 10 mM imidazole and TBS + 30 mM imidazole. Protein was eluted with 5 CV of TBS + 500 mM imidazole and further purified on a HiTrap Heparin HP 5 ml (Cytiva) in TBS. Protein was then eluted with a 200–1,000 mM NaCl gradient in TBS over 20 CV. The target protein containing fractions were pooled, concentrated to 1 ml (Amicon 15 ml, molecular weight cutoff 30 kDa) and finally purified by Superdex 200 Increase 10/300 GL SEC column (Cytiva) using buffer containing 10 mM Tris pH 8.0 and 150 mM NaCl buffer. Peak fractions corresponding to target protein were pooled, flash frozen in liquid nitrogen and stored at −80 °C until use.

Negative staining electron microscopy

For negative staining, an aliquot of 5 µl of purified Flag-NAIP5 (0.1 mg ml^{-1}) from the void fraction or monomeric fraction was applied onto a glow-discharged copper grid (FCF400-Cu, Electron Microscopy Sciences, EMS) and kept for 1 min. Excess was blotted with filter paper, next immediately stained with 2% uranyl acetate (5 µl, EMS no. 22400) for 30 s, the excess was blotted and the grid was air-dried. The grids were imaged under an FEI Tecnai Transmission Electron Microscope equipped with a 5 megapixel CCD camera.

Cryo-EM sample preparation and data collection

The purified Flag-NAIP5 (0.3 mg ml^{-1}) was loaded onto a glow-discharged UltrAuFoil grid (R1.2/1.3 300-mesh, Electron Microscopy Sciences no. Q350AR13A). Vitrification was performed using Mark IV Vitrobot (Thermo Fisher) with 3–5 s blot time under 100% humidity at 4 °C. These vitrification conditions were optimized through screening on Arctica to check ice thickness and particle distribution, the best grids were used for data collection on a Titan Krios (Thermo Fisher) equipped with BioQuantum Imaging Filter (Gatan Inc., slit width 20 eV) and K3 Summit direct electron detector (Gatan Inc.). All videos were automatically collected using serialEM[39] at nominal magnification ×81,000 (super-resolution pixel size 0.5347 Å) with a total dose of 52 e$^-$/Å^2, and were then fractionated into 52 frames. Defocus range was set from 1.0 to 2.5 µm for all datasets: 3,682 images were collected at 0° and 1,597 at 30° stage tilt.

Cryo-EM data processing and atomic model refinement

Data processing and reconstruction were performed with Relion[22] and cryoSPARC[23]. Video stacks were aligned and summed with frames 2–51 using Patch motion correction without binning. Contrast tranfer function (CTF) estimation was performed using Patch CTF. Micrographs with CTF fit resolution better than 5 Å were selected for further processing. A total number of 566,945 particles were initially picked from 462 micrographs with a blob picker and subjected to 2D classification to generate templates for the Template picker, with 4,354,235 particles from 0° tilt and 3,690,207 particles from 30° tilt that were obtained from the entire dataset. After several rounds of 2D classification with Relion[22] and ab initio reconstruction and heterogeneous refinement with cryoSPARC[23], a final 197,597 particles from 0° tilt and 133,370 particles from 30° tilt were collected and used to create an initial model (*K* = 3). Then multiple rounds of heterogeneous refinement and further 2D classification were performed, bad particles were removed, 36,523 particles from the tilted dataset and 122,990 particles from the untilted dataset were subjected to nonuniform refinement and homogeneous refinement. The resulting maps were subjected to postprocessing with deepEMhancer[40]. The directional Fourier shell correlation (FSC) plot and sphericity of nonuniform refinement map was measured as in ref. [41].

For building the atomic model of unliganded NAIP5, the individual domains of AlphaFold predicted structure were split (NTD 1–60; BIR1 61–135; BIR2 136–245; BIR3 246–403; NBD 404–600; HD1 601–660; WHD 661–760; HD2 761–889; LRR 920–1403) and rigidly docked into

our cryo-EM map in UCSF Chimera[42]. The density fitnesses of residues were manually inspected and adjusted in COOT[25] and refined with multiple cycles of PHENIX real space refinement[26,43]. Figures are generated with Pymol (The PyMOL Molecular Graphics System, v.1.7 Schrödinger, LLC.).

NAIP5–NLRC4 inflammasome assay

The inflammasome assay was performed as previously described with some modifications[3,4], all experiments were repeated three times. Briefly, plasmids of pCMV-mPro-IL-1β (100 ng, Addgene no. 73953, a gift from C. Stehlik[44]), pCMV-mCaspase1-C-flag (10 ng, Addgene no. 21142, a gift from J. Yuan[45]), pCS2-Myc-NLRC4 (300 ng, a gift from F. Shao), pcDNA3.4-Flag-NAIP5 WT/mutant (300 ng) were cotransfected into HEK293T cells (gifted from X. Xiao) in a 12-well plate. After 24 h of transfection, LFn-FlaA and protective antigen proteins were added to the culture medium to a final concentration of 10 µg ml^{-1}. The same concentrations of LFn-FlaAAA and protective antigen were added to the negative control well. After another 24 h, the transfected cells were gathered in a passive lysis buffer (250 µl per well; Promega no. E194A) and obtained supernatants were subjected to western blot analysis. The detection of cleaved IL-1β (p17) on an immunoblot confirmed the occurrence of active inflammasome complex formation. Antibodies used were: anti-IL-1 (Abcam no. 234437), anti-Flag (Sigma no. F1804), anti-Myc (Cell Signaling no. 2276), anti-Caspase-1 (Cell Signaling no. 24232), antimouse IgG (Cell Signaling no. 7076), antirabbit IgG (Cell Signaling no. 7074S) and anti-β-tubulin (Invitrogen no. MA5-16308-HRP).

Blue native–PAGE

HEK293T cells in a 12-well plate were transfected with Flag-NAIP5 and MBP-NLRC4. Ligand (FliC/FlaA) was introduced either by cotransfection (using plasmid pCMV-His-FliC or pCMV-His-FliCD0$_L$) or by translocation (using proteins LFn-FlaA and PA) after 24 h of transfection. Eventually, cells were gathered after a total time of 48 h and washed with ice-cold PBS, followed by addition of a previously optimized lysis buffer containing 1% digitonin[4]. Clarified cell lysates were subjected to 3–12% blue native–PAGE as per the manufacturer's recommendations (NativePAGE Novex Bis-Tris Gel System, Thermo Fisher Scientific), followed by western blots against specific antibodies (as mentioned above).

In vitro pulldown assay

Expi293F cells (50 ml at 3 million cells per ml) were cotransfected with pcDNA3.4-Flag-NAIP5 WT/mutant and pBackman-MBP-NLRC4 (delta CARD), either with or without pCMV-His-FliC, and then cultured for 72 h before collection. Cell lysis was performed in the buffer containing 50 mM HEPES, pH 7.6, 150 mM NaCl, 10 mM KCl, 5 mM MgCl$_2$, 5% glycerol, 1% Triton-X-100, 1× protease inhibitor cocktail and the obtained lysate (10 ml) was subjected to pulldown on splitting into halves. One half was incubated with amylose resin (0.1 ml, New England Biolabs, NEB no. E8021L) and the other with anti-flag M2 affinity resin (0.1 ml, Sigma) for 2 h at 4 °C at constant rotational shaking. Supernatant was removed and resin was washed with the buffer containing 50 mM HEPES pH 7.6, 150 mM NaCl, 10 mM KCl, 5 mM MgCl$_2$, 5% glycerol, 0.02% NP-40A and the bound protein was eluted in the same buffer with a specific competitive agent for each resin (25 mM maltose for amylose resin; 150 µg ml^{-1} 3× flag peptide for anti-flag resin). Samples were subjected to immunoblotting with anti-MBP (NEB no. E8032S) and anti-Flag (Sigma no. F1804), and all experiments were repeated three times.

ATPase activity assay for NAIP5

The assay was performed using ATPase/GTPase activity assay kit (Sigma no. MAK113) in 96-well plates as per the manufacturer's recommendations. Flag-NAIP5 used for ATPase assay was also purified in a similar wat

to the above mentioned protocol but using the assay buffer consists of 50 mM HEPES pH 7.6, 150 mM NaCl, 10 mM KCl, 5 mM MgCl$_2$, 5% glycerol, 0.02% NP-40A, 1 mM TCEP. Bovine serum albumin in assay buffer was used as a negative control. Reaction samples containing protein ranging from 0 to 30 µM were prepared in a 20 µl volume, and then mixed with an equal volume of reaction mixture containing 2 mM ATP (Sigma no. A1852) in assay buffer and incubated for 1 h at room temperature. The reaction was stopped by adding 200 µl of malachite green reagent, and further incubating for 30 min at room temperature before measuring absorbance at 620 nm. For estimation of the free phosphate concentration, a linear regression was generated using free phosphate standards in assay buffer. One unit of ATPase activity is defined as the amount of enzyme that catalyzes the production of 1 µM of free phosphate per minute under the assay conditions, as instructed by the assay kit.

Reporting summary

Further information on research design is available in the Nature Portfolio Reporting Summary linked to this article.

Data availability

The cryo-EM maps were deposited in the Electron Microscopy Data Bank under the accession IDs EMD-24387 (3.3 Å) and EMD-24389 (3.6 Å), and the atomic coordinates were deposited in the PDB under the accession ID 7RAV. Plasmids are available from the corresponding author. Source data are provided with this paper.

References

38. Erijman, A., Dantes, A., Bernheim, R., Shifman, J. M. & Peleg, Y. Transfer-PCR (TPCR): a highway for DNA cloning and protein engineering. *J. Struct. Biol.* **175**, 171–177 (2011).
39. Mastronarde, D. N. Automated electron microscope tomography using robust prediction of specimen movements. *J. Struct. Biol.* **152**, 36–51 (2005).
40. Sanchez-Garcia, R. et al. DeepEMhancer: a deep learning solution for cryo-EM volume post-processing. Preprint at *bioRxiv* https://doi.org/10.1101/2020.06.12.148296 (2020).
41. Tan, Y. Z. et al. Addressing preferred specimen orientation in single-particle cryo-EM through tilting. *Nat. Methods* **14**, 793–796 (2017).
42. Pettersen, E. F. et al. UCSF Chimera–a visualization system for exploratory research and analysis. *J. Comput. Chem.* **25**, 1605–1612 (2004).
43. Liebschner, D. et al. Macromolecular structure determination using X-rays, neutrons and electrons: recent developments in Phenix. *Acta Crystallogr. D. Struct. Biol.* **75**, 861–877 (2019).
44. Bryan, N. B., Dorfleutner, A., Rojanasakul, Y. & Stehlik, C. Activation of inflammasomes requires intracellular redistribution of the apoptotic speck-like protein containing a caspase recruitment domain. *J. Immunol.* **182**, 3173–3182 (2009).
45. Li, J., Yin, H. L. & Yuan, J. Flightless-I regulates proinflammatory caspases by selectively modulating intracellular localization and caspase activity. *J. Cell Biol.* **181**, 321–333 (2008).

Acknowledgements

Author contributions

L.Z., B.P. and J.C. conceived the study. B.P. purified the protein and performed negative stain EM analysis. J.C. made cryo-grids and collected cryo-EM data. L.Z. and J.C. performed data processing. L.Z. performed initial model building, B.P. and Q.X. performed additional refinement. L.Z. and B.P. designed mutants for functional assays, B.P. performed biochemical assays, G.N. did technical replicates. L.Z., B.P., J.C., G.N. and H.W. wrote the manuscript.

Competing interests

H.W. is a cofounder of Ventus Therapeutics. The other authors declare no competing interests.
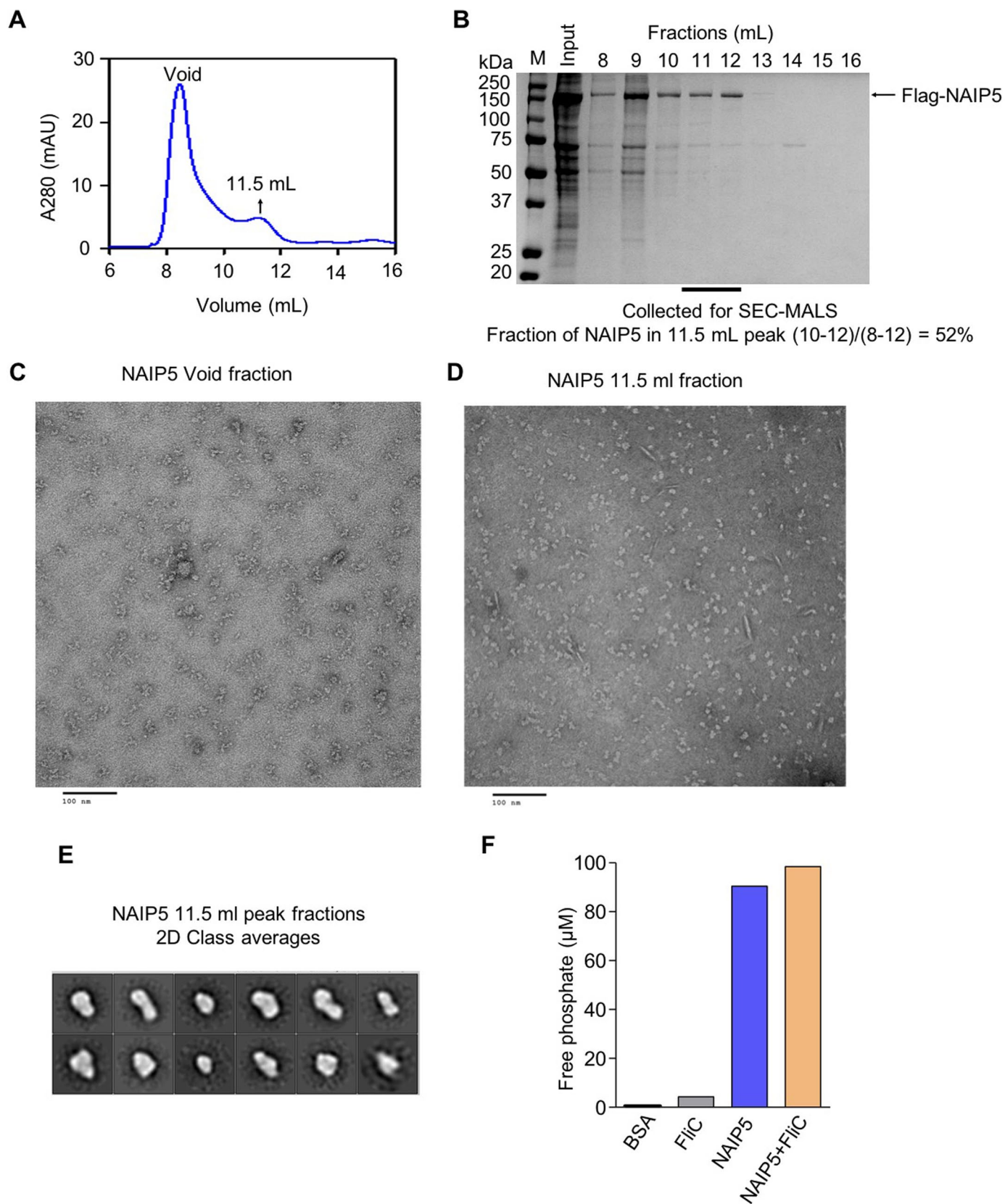
Additional information

Extended data is available for this paper at https://doi.org/10.1038/s41594-022-00889-2.

Supplementary information The online version contains supplementary material available at https://doi.org/10.1038/s41594-022-00889-2.

**Correspondence and requests for materials** should be addressed to Liman Zhang.

Peer review information *Nature Structural & Molecular Biology* thanks Jun Ma, Edward Miao and the other, anonymous, reviewer(s) for their contribution to the peer review of this work. Primary Handling Editor: Carolina Perdigoto, in collaboration with the *Nature Structural & Molecular Biology* team. Peer reviewer reports are available.

Reprints and permissions information is available at www.nature.com/reprints.

A

B

Collected for SEC-MALS
Fraction of NAIP5 in 11.5 mL peak (10-12)/(8-12) = 52%

C NAIP5 Void fraction

D NAIP5 11.5 ml fraction

E

NAIP5 11.5 ml peak fractions
2D Class averages

F

Extended Data Fig. 1 | Superdex-200 profile of the recombinant Flag-NAIP5 and Negative stain EM for void and monomeric fractions. a) Size exclusion chromatography profile of Flag-NAIP5; **b**) SDS-PAGE for fractions from A). Densitometric analysis was performed using Bio-Rad Image Lab Software 6.1 to calculate the fraction of 11.5 ml peak; This experiment was repeated three independent times. **c**) Negative stain EM image for the Superdex200 fraction eluted from the void peak as shown in B); **d**) Negative stain EM image for the 11.5 mL Superdex200 fraction as shown in B); **e**) 2D class averages of particles picked from D). **f**) Repetition of Fig. 2e with separately purified batches of protein showing FliC does not enhance the ATPase activity of NAIP5.
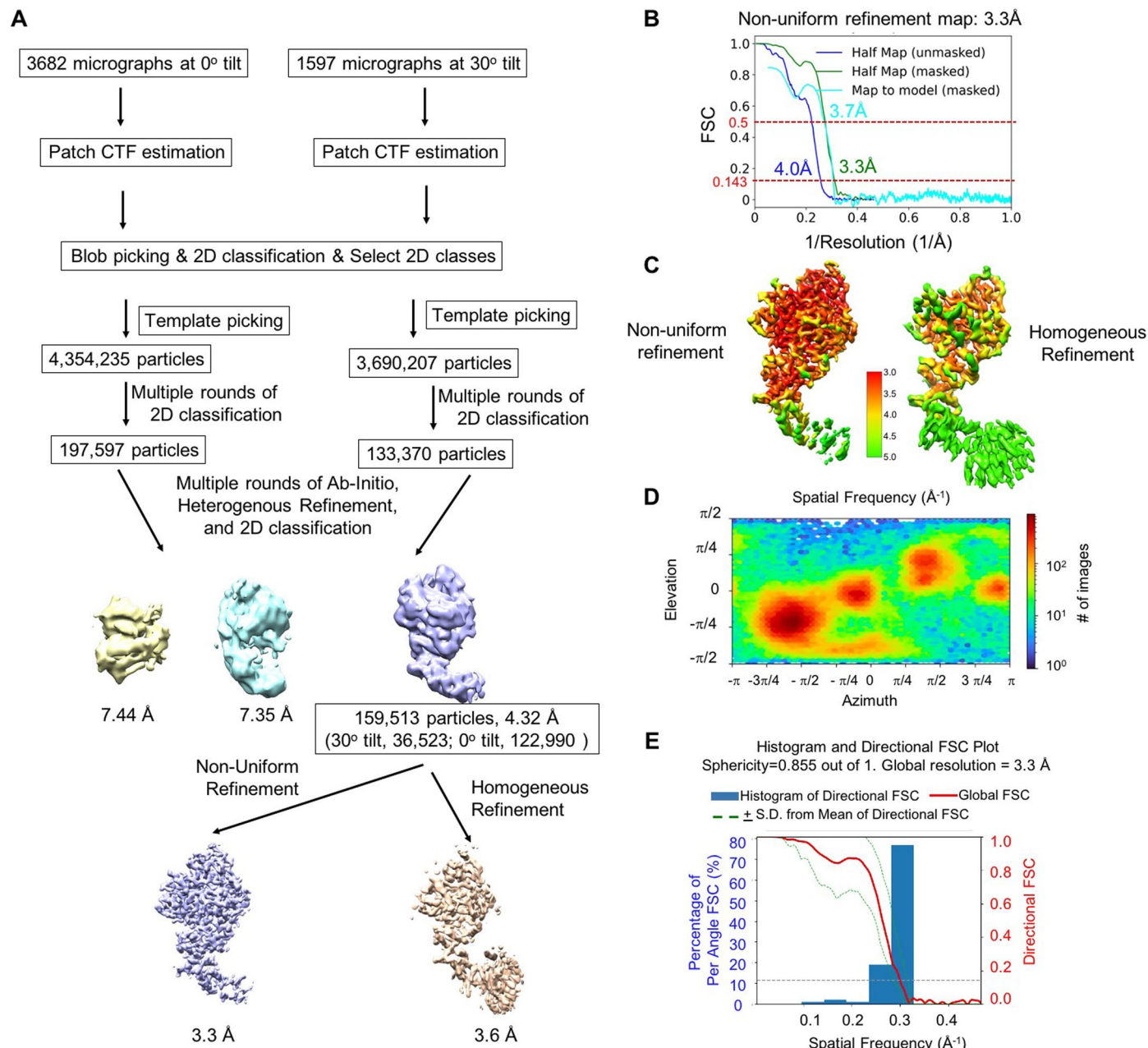
Extended Data Fig. 2 | Cryo-EM data processing and reconstruction. a) Schematic workflow of 2D/3D classification and reconstruction. In total, we completed 6 rounds of 3D classification interleaved with 2D classification in each 3D class. After each round of 3D and 2D classification, bad classes were rejected by visual inspection. We obtained 159,513 particles for final refinement, with 36,523 particles from the tilted dataset and 122,990 particles from the un-tilted dataset; **b)** The gold-standard Fourier Shell Correlation (FSC) plots of the cryo-EM map obtained from non-uniform refinement. FSC curve for the cross-validation of the atomic models of the inactive NAIP5 is also showed; **c)** The EM density maps of the Non-uniform refinement and Homogeneous refinement with color coded to show the local resolution as calculated by cryoSPARC. **d)** Orientation distribution map of Non-uniform and Homogeneous refinement. **e)** Plots of the global half-map FSC (solid red line) together with the spread of directional resolution values (green area encompassed by dotted green lines, left axis), and histogram of directional FSC (blue bars).
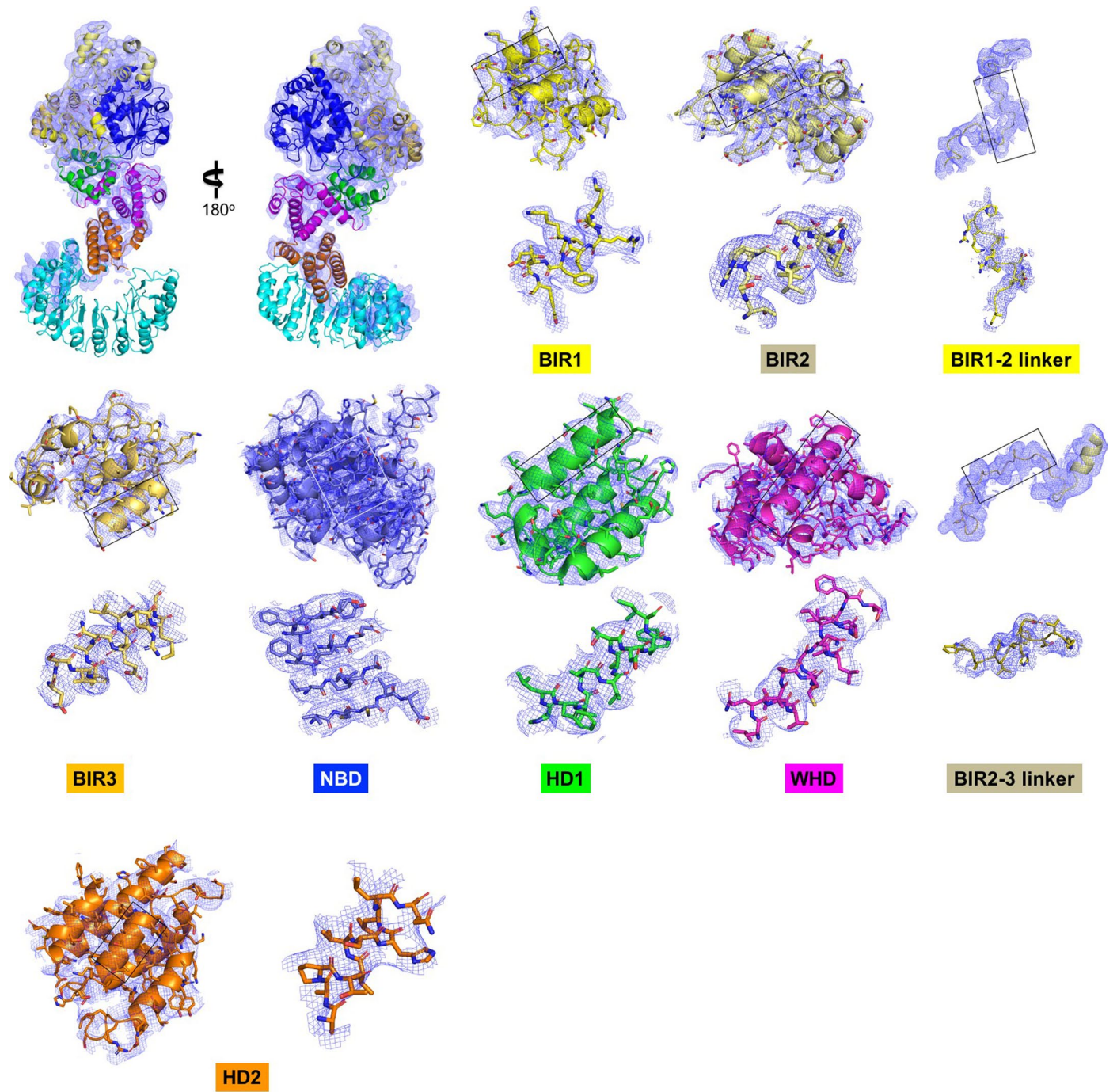
Extended Data Fig. 3 | Representative EM densities of pre-liganded NAIP5. EM densities and their corresponding models are shown for the individual domains of pre-liganded NAIP5.
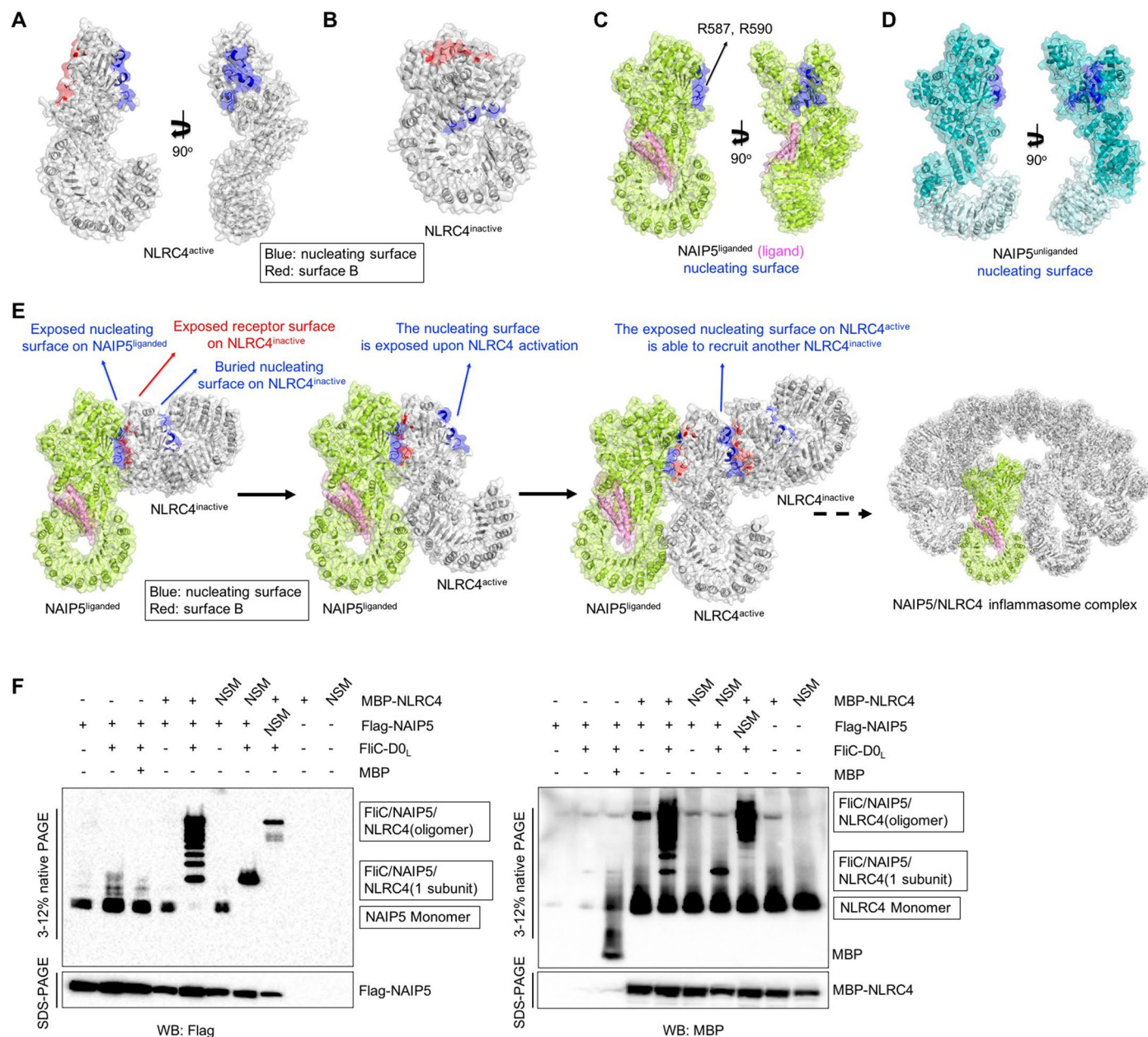
Extended Data Fig. 4 | NAIP5 depended NLRC4 activation. a) the nucleating surface (blue) and receptor surface (red) in the active NLRC4; **b**) The nucleating surface (blue) and receptor surface (red) in the inactive NLRC4; **c**) The exposed nucleating surface (blue) on ligand-bound NAIP5; **d**) The exposed nucleating surface (blue) on pre-liganded NAIP5; **e**) NLRC4 is recruited to NAIP5 by NAIP5-nucleating surface, and NLRC4- nucleating surface is exposed upon NLRC4 activation to initiate a domino-like process to form inflammasome complex; **f**) Only in the presence of ligand (FliC-D0$_L$, the smallest FliC fragment effective in activating NAIP5), NAIP5 is able to induce NLRC4 oligomerization, or form a complex with 1 subunit of NLRC4 nucleation surface mutant (NSM), which is deficient in further oligomerization. This experiment was repeated three independent times.
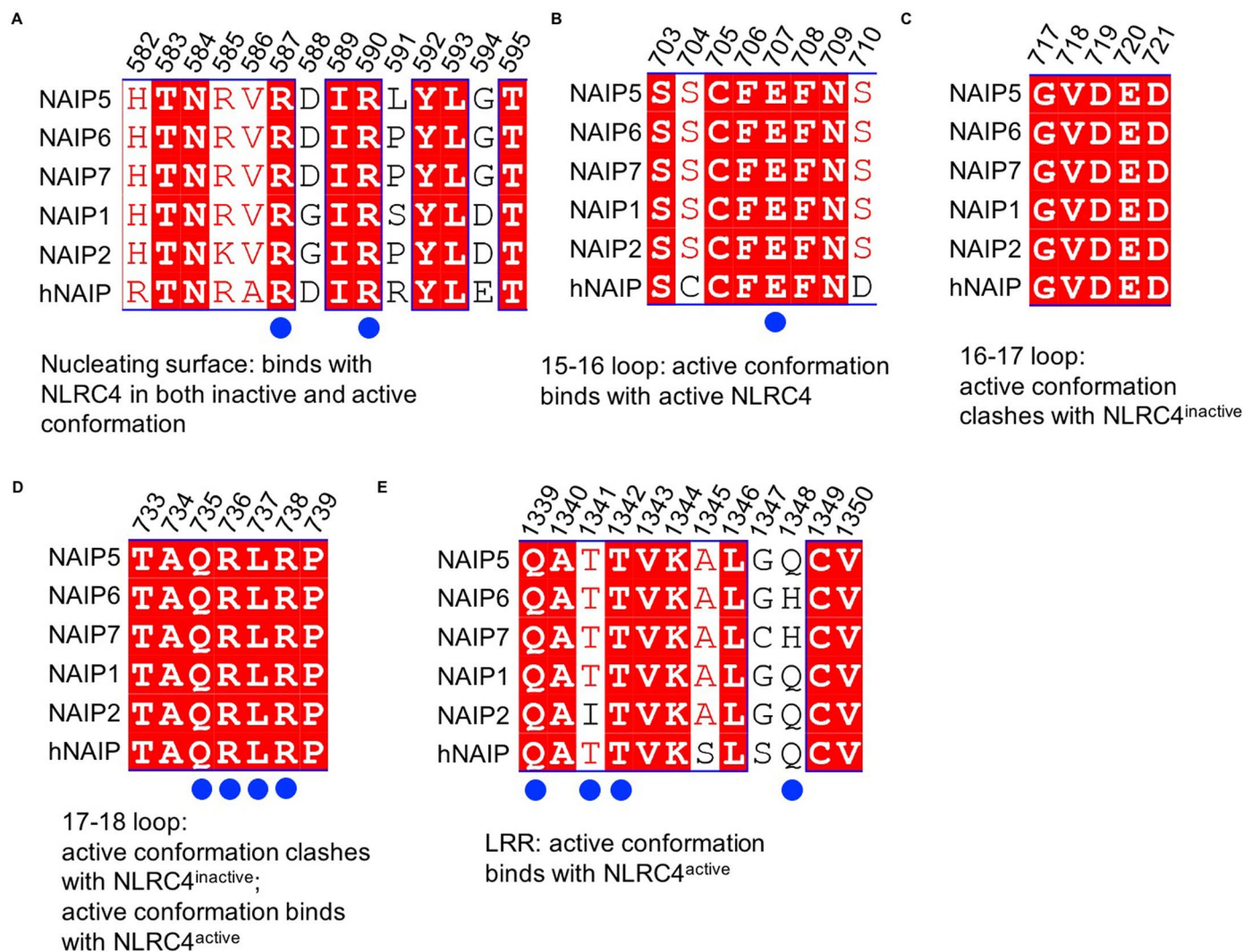
Extended Data Fig. 5 | Sequence alignment of the key regions discussed in this work. Conserved and similar residues are highlighted in white and red. The blue circles indicate residues tested by mutagenesis. Amino acid numbering corresponds to NAIP5 was given on the top of the alignment.

Corresponding author(s): Liman Zhang

Last updated by author(s): Oct 20, 2022

Reporting Summary

Nature Portfolio wishes to improve the reproducibility of the work that we publish. This form provides structure for consistency and transparency in reporting. For further information on Nature Portfolio policies, see our Editorial Policies and the Editorial Policy Checklist.

Statistics

For all statistical analyses, confirm that the following items are present in the figure legend, table legend, main text, or Methods section.

n/a	Confirmed	
☐	☒	The exact sample size (*n*) for each experimental group/condition, given as a discrete number and unit of measurement
☐	☒	A statement on whether measurements were taken from distinct samples or whether the same sample was measured repeatedly
☒	☐	The statistical test(s) used AND whether they are one- or two-sided *Only common tests should be described solely by name; describe more complex techniques in the Methods section.*
☒	☐	A description of all covariates tested
☒	☐	A description of any assumptions or corrections, such as tests of normality and adjustment for multiple comparisons
☒	☐	A full description of the statistical parameters including central tendency (e.g. means) or other basic estimates (e.g. regression coefficient) AND variation (e.g. standard deviation) or associated estimates of uncertainty (e.g. confidence intervals)
☒	☐	For null hypothesis testing, the test statistic (e.g. *F*, *t*, *r*) with confidence intervals, effect sizes, degrees of freedom and *P* value noted *Give P values as exact values whenever suitable.*
☒	☐	For Bayesian analysis, information on the choice of priors and Markov chain Monte Carlo settings
☒	☐	For hierarchical and complex designs, identification of the appropriate level for tests and full reporting of outcomes
☒	☐	Estimates of effect sizes (e.g. Cohen's *d*, Pearson's *r*), indicating how they were calculated

Our web collection on statistics for biologists contains articles on many of the points above.

Software and code

Policy information about availability of computer code

Data collection	serial EM
Data analysis	CryoSparc 3.3.1, Relion 3.1, DeepEMhancer 0.13, Phenix 1.18.2, Coot 0.9.4.1, Pymol 1.7

For manuscripts utilizing custom algorithms or software that are central to the research but not yet described in published literature, software must be made available to editors and reviewers. We strongly encourage code deposition in a community repository (e.g. GitHub). See the Nature Portfolio guidelines for submitting code & software for further information.

Data

Policy information about availability of data

All manuscripts must include a data availability statement. This statement should provide the following information, where applicable:

- Accession codes, unique identifiers, or web links for publicly available datasets
- A description of any restrictions on data availability
- For clinical datasets or third party data, please ensure that the statement adheres to our policy

The cryo-EM maps were deposited in the Electron Microscopy Data Bank under the accession IDs: EMD-24387 (3.3 Å), EMD-24389 (3.6 Å) and the atomic coordinates were deposited in the Protein Data Bank under the accession ID: 7RAV. Plasmids are available from the corresponding author.

Field-specific reporting

Please select the one below that is the best fit for your research. If you are not sure, read the appropriate sections before making your selection.

☒ Life sciences   ☐ Behavioural & social sciences   ☐ Ecological, evolutionary & environmental sciences

For a reference copy of the document with all sections, see nature.com/documents/nr-reporting-summary-flat.pdf

Life sciences study design

All studies must disclose on these points even when the disclosure is negative.

Sample size	The cryoEM data size was determined by the ability to reach a resolution in the WHD better than 3.5Å
Data exclusions	No data were excluded from the analysis of assays.
Replication	All attempts at replication were successful. Inflammasomal assay, BN-PAGE, pull-down, and ATPase Activity Assay were repeated at least three times. purification and analysis of cryoEM samples were also repeated at least three times.
Randomization	No randomization was performed.
Blinding	Blinding was not necessary for cryoEM studies and inflammasomal assay because there is no subjective evaluation of the assay results.

Reporting for specific materials, systems and methods

We require information from authors about some types of materials, experimental systems and methods used in many studies. Here, indicate whether each material, system or method listed is relevant to your study. If you are not sure if a list item applies to your research, read the appropriate section before selecting a response.

Materials & experimental systems

n/a	Involved in the study
☐	☒ Antibodies
☐	☒ Eukaryotic cell lines
☒	☐ Palaeontology and archaeology
☒	☐ Animals and other organisms
☒	☐ Human research participants
☒	☐ Clinical data
☒	☐ Dual use research of concern

Methods

n/a	Involved in the study
☒	☐ ChIP-seq
☒	☐ Flow cytometry
☒	☐ MRI-based neuroimaging

Antibodies

Antibodies used	anti-IL-1 (abcam #234437, dilution factor 1:1000), anti-Flag (Sigma #F1804, dilution factor 1:1000), anti-Myc (Cell signaling # #2276, dilution factor 1:1000), anti-Caspase-1(AdipoGen #AG-20B-0042-C100, dilution factor 1:1000), anti-β-tubulin (Invitrogen #MA5-16308-HRP, dilution factor 1:1000), and anti-MBP (NEB # E8032S, dilution factor 1:10000)
Validation	Validation of antibodies used in this research are provided on the manufacturers' website.

Anti-IL-1 (abcam #234437) was tested Reacts with Mouse IL-1b and suitable for WB, ICC/IF, IP, Flow Cyt, Unsuitable for: IHC-P;

anti-Flag M2 mouse(Sigma #F1804), affinity purified monoclonal antibody binds to fusion proteins containing a FLAG peptide sequence.The antibody recognizes the FLAG peptide sequence at the N-terminus, Met-N-terminus,C-terminus, and internal sites of the fusion protein.

anti-Myc (Cell signaling # #2276) is recommended for detection of c-Myc p67 and c-Myc tagged fusion proteins of mouse, rat, human, monkey, feline and canine origin by WB, IP, IF, IHC(P), FCM and ELISA; non cross-reactive with N-Myc or L-Myc proteins. Widely used in combination with eukaryotic expression vectors encoding proteins with c-Myc (amino acids 408-439) epitope tag.

anti-Caspase-1(AdipoGen #AG-20B-0042-C100) recognizes endogenous full-length and activated (p20 fragment) mouse caspase-1. Described to cross-react with full-length and activated (p20 fragment) of rat caspase-1 (Lit. #30 & 34).

anti-β-tubulin (Invitrogen #MA5-16308-HRP) can be used in several scientific applications, including Immunocytochemistry, Western Blot, Immunohistochemistry, Immunoprecipitation and ELISA. These antibodies target alpha Tubulin in Human, Mouse, Rat, Porcine and Canine samples. |

anti-MBP (NEB # E8032S) is a murine anti-maltose binding protein (MBP) antibody, isotype IgG2a, verified for use in both Western blotting and ELISA.

Eukaryotic cell lines

Policy information about cell lines

Cell line source(s)	HEK293T was obtained from ATCC and Expi293 was purchased from Thermofisher
Authentication	Authentication are performed by the manufacture, successful performance of protein expression from these strains authenticates them.
Mycoplasma contamination	No mycoplasma contamination was observed.
Commonly misidentified lines (See ICLAC register)	no commonly misidentified cell lines were used in the study.